Stability Enhancement Based on Virtual Impedance for DC Microgrids With Constant Power Loads — Source link

Xiaonan Lu, Kai Sun, Josep M. Guerrero, Juan C. Vasquez ...+2 more authors

Institutions: Argonne National Laboratory, Tsinghua University, Aalborg University

Related papers:

- Dynamic Behavior and Stabilization of DC Microgrids With Instantaneous Constant-Power Loads

- A Novel Stabilization Method of LC Input Filter With Constant Power Loads Without Load Performance Compromise in DC Microgrids

- Constant power loads and negative impedance instability in automotive systems: definition, modeling, stability, and control of power electronic converters and motor drives

- DC Microgrids—Part I: A Review of Control Strategies and Stabilization Techniques

- Constant-Power Load System Stabilization by Passive Damping

Aalborg Universitet

AALBORG UNIVERSITY

DENMARK

Stability Enhancement Based on Virtual Impedance for DC Microgrids with Constant Power Loads

Lu, Xiaonan; Sun, Kai; Guerrero, Josep M.; Quintero, Juan Carlos Vasquez; Huang, Lipei; Wang, Jianhui

Stability Enhancement Based on Virtual Impedance for DC Microgrids with Constant Power Loads

Xiaonan Lu, *Member*, *IEEE*, Kai Sun, *Member*, *IEEE*, Josep M. Guerrero, *Fellow*, *IEEE*, Juan C. Vasquez, *Senior Member*, *IEEE*, Lipei Huang, Jianhui Wang, *Senior Member*, *IEEE*

Abstract - **In this paper, a converter-based DC microgrid is studied. By considering the impact of each component in DC microgrids on system stability, a multi-stage configuration is employed, which includes the source stage, interface converter stage between buses and common load stage. In order to study the overall stability of the above DC microgrid with constant power loads (CPLs), a comprehensive small-signal model is derived by analyzing the interface converters in each stage. The instability issue induced by the CPLs is revealed by using the criteria of impedance matching. Meanwhile, virtual-impedance-based stabilizers are proposed in order to enhance the damping of DC microgrids with CPLs and guarantee the stable operation. Since droop control is commonly used to reach proper load power sharing in DC microgrids, its impact is taken into account when testing the proposed stabilizers. By using the proposed stabilizers, virtual impedances are employed in the output filters of the interface converters in the second stage of the multi-stage configuration. In particular, one of the virtual impedances is connected in series with the filter capacitor, and the other one is connected at the output path of the converter. It can be seen that by using the proposed stabilizers, the unstable poles induced by the CPLs are forced to move into the stable region. The proposed method is verified by the MATLAB/Simulink model of multi-stage DC microgrids with three distributed power generation units.**

***Index Terms* - constant power load, DC microgrid, stability, virtual impedance**

I. INTRODUCTION

With the increasing penetration of renewable energy into modern electric grid, the concept of microgrid was proposed several years ago [1]. During the recent years, microgrids have been widely studied. Since the conventional electric grid relies on AC, the research on microgrids are mainly focused on AC systems [2]-[7]. However, in order to integrate various renewable energy sources with DC couplings, the solution of DC microgrids has become an attracting approach [8]-[10]. In contrast with AC microgrids, DC microgrids have drawn growing concerns for the advantages of higher efficiency, absence of reactive power and harmonics, etc [9]-[10]. In a DC microgrid, the renewable energy sources are connected to the common bus by using the interface converters [11]-[16]. Considering the distributed configuration of the system, power electronics interface converters are usually connected in parallel. In order to obtain proper load power sharing among different sources, droop control as a decentralized method is commonly employed in the control diagram of the interface converters [12]-[16]. A typical DC microgrid is depicted in Fig. 1.
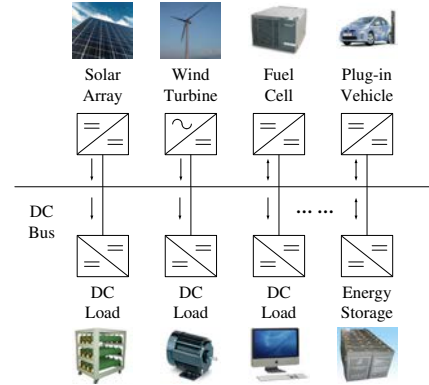
Fig. 1. Typical configuration of DC microgrids.

Stability issues should be noticed to enhance the performance of a DC microgrid. Especially in the system with constant power loads (CPLs), the stability issues are required to be further studied. In a microgrid, the CPL, also known as active load, enables the power conditioning at the load side. Different from passive loads, CPLs, e.g. DC motor, energy storage charged by constant power, etc., consume constant amount of power regardless what the input voltage is. It should be noted that the behavior of a converter-dominated load is determined by the corresponding control. For instance, for a point-of-load (POL) converter with a resistor connected at its output terminal, if the load converter is in voltage control mode to ensure a fixed voltage across the load resistor, the entirety of the POL converter and its resistor load can be regarded as a CPL. CPLs can be found in many applications, e.g. aircrafts [17]-[18], ships [19] and microgrids [20]. The impact of CPL on the system stability is induced by its

negative impedance in the small signal analysis. The negative incremental impedance makes the system poorly damped and can induce instable poles in the frequency domain. Therefore, the system stability is degraded [21]-[22]. The above issue induced by CPL has been studied extensively, as shown in the literature review in Section II. Considering that DC microgrid is the research focus of this paper, since multiple interface converters usually co-exist and they are connected in parallel, it is necessary to derive a comprehensive system model that includes different components of a DC microgrid and extend the research on CPL and its damping method to multiple converter system. Meanwhile, the commonly used droop control should be taken into account when discussing the stabilization of the microgrid with CPLs.

Virtual impedances have obtained increasing awareness in the control diagram of the interface converters nowadays. They have generally two functionalities. First, virtual impedances can be used to match the grid-side impedance in AC microgrids. The sharing of output active and reactive power can be thereby efficiently decoupled [23]. Furthermore, the virtual impedance can be programmed at the certain frequency to form the expected harmonic impedance, which enables the function of harmonic sharing and damping [24]. Second, virtual impedances can be employed to realize the resonance damping in the LCL filters [25]. By using the additional current sensors and multiple control loops, the resonance peaks imposed by LCL filters can be attenuated.

Diverse types of configurations can be found in the existing DC microgrids. The single bus system in [26] is commonly used in small-scale DC microgrids, which is comprised of renewable energy sources with stochastic output power, e.g. photovoltaic (PV), wind turbines, etc., and energy storage as energy buffer to establish the bus voltage. The PVs and wind turbines commonly operate in power output mode to absorb maximum power, and the energy storage operates in voltage output mode to establish the common bus voltage. For larger-scale DC microgrids, the above single bus system can be extended to a multi-bus system [14]. In a DC microgrid with multiple buses, different local DC buses are collected at point-of-common-coupling (PCC) through transmission lines. Meanwhile, the original single bus can be regarded as source bus with combined renewable energy sources.

In this paper, virtual-impedance-based stabilizers for DC microgrids with CPLs is proposed. Without loss of generality, a multi-stage configuration of DC microgrid is employed, which is comprised of three stages. The first stage is the source stage where combined sources of PV and battery are utilized to establish the source bus. Similar to the single bus system, the PV works in maximum power point tracking (MPPT) mode and the battery works in voltage output mode to build the bus voltage. By considering the stochastic output power of PV and load condition, sizing of the battery can be properly accomplished to guarantee the stable source bus voltage. The second stage is the local interface converter stage. The input of the interface converter is the source bus with stable voltage, and the output is the local output bus. The virtual-impedance-based stabilizers are employed in the control diagram of the interface converters in this stage. Meanwhile, droop control is also used to achieve proper power sharing among different converters. Meanwhile, the transmission line connected to each local output bus is also included in this stage. The third stage is the load stage which includes the common load bus. Here, in order to study the impact of CPL and develop the related damping method, CPLs are connected at the PCC in the third stage. Among the above three stages, the first and second stage features distributed configuration, which can be regarded as distributed power generation units, and the third stage includes the common bus where different distributed units are collected. In order to study the overall system stability, a comprehensive small-signal model of the whole system comprised of the above three stages is derived. Based on the derived model, the stability analysis considering the impacts of CPL and the proposed stabilizers are performed. Based on the derived systematic model of DC microgrids with multiple distributed power generation units, virtual-impedance-based stabilizers are implemented in Stage II. Virtual impedances at two positions in the output side of the interface converters are realized to tackle the instability issues induced by CPLs. Since the virtual-impedance-based stabilizers are located at two positions, higher control flexibility can be achieved compared to conventional approaches based on single virtual impedance. Impedance criteria is selected as a tool to evaluate the overall system stability with the virtual-impedance-based stabilizers [27]. In particular, the above multi-stage DC microgrid is divided into two sections, i.e. the local source section and common load section. The local source section is comprised of Stage I and II, while the common load section is comprised of Stage III. The output impedance of the local source section, namely Z_s, and the input impedance of the common load section including CPL, namely Z_l, are calculated. By using the criteria of impedance matching, the overall system stability is evaluated by the dominant poles of $(1+Z_s/Z_l)^{-1}$. When all the dominant poles locate in the stable region, the system stability is guaranteed. The proposed virtual-impedance-based stabilizers are employed to move the instable poles into the stable region.

The contribution of our paper can be summarized as follows. A comprehensive system model for DC microgrids is derived by considering three stages, i.e. source stage, interface converter stage and load stage. The dynamics involved in each stage and the impact of droop control are taken into account. The proposed model is specially developed for DC microgrids with multiple distributed energy generation units. Meanwhile, virtual-impedance-based stabilizers are employed in each distributed power generation unit. In particular, the virtual-impedance-based stabilizers are located at two positions. One of them is connected in series with the DC-link capacitor of the interface converter, while the other one is connected at the output path of the converter. Both of them are located at the generation side. The combination of the virtual stabilizers at two positions allows higher flexibility of the control diagram.

The following paper is organized as follows. Section II

briefly investigates the impact of CPL on system stability, and a literature survey of related damping method is conducted. Section III discusses the configuration of multi-stage DC microgrid and the comprehensive small-signal model for the whole system is derived. Based on this model, the stability analysis is performed by using impedance matching criteria with consideration of the proposed virtual-impedance-based stabilizers. Section IV shows the simulation results derived from MATLAB/Simulink model to demonstrate the proposed approach. Finally, Section V summarizes the paper and draws the conclusion.

II. REVIEW OF STABILITY ISSUES INDUCED BY CPLS AND CORRESPONDING DAMPING METHODS

For the constant power nature of the load, the following expression is satisfied:

$$P_1 = v_1 \cdot i_1 \tag{1}$$

where v_1, i_1 and P_1 are the voltage, current and power of a CPL.

The incremental impedance of the CPL can be calculated as follows if neglecting the interactions between the load converter and its upstream converters [28]-[29]:

$$\frac{\partial v_{\text{load}}}{\partial i_{\text{load}}}\bigg|_{(V_{\text{load}},I_{\text{load}})} = \frac{\partial}{\partial i_{\text{load}}}\left(\frac{P_{\text{load}}}{i_{\text{load}}}\right)\bigg|_{(V_{\text{load}},I_{\text{load}})} = -\frac{P_{\text{load}}}{I_{\text{load}}^2} = -\frac{V_{\text{load}}}{I_{\text{load}}} \tag{2}$$

It is seen from (2) that the CPL has negative incremental impedance, which makes the system less damped and impacts the system stability. The same phenomenon can be found in the *I-V* curve of the load, as shown in Fig. 2. It is seen that for the CPL, the product of the load voltage and current are constant. Hence, the *I-V* curve satisfies the characteristic of inverse proportional function. As a result, the slope at the operating point (V_1, I_1) is negative, which indicates the negative incremental impedance.
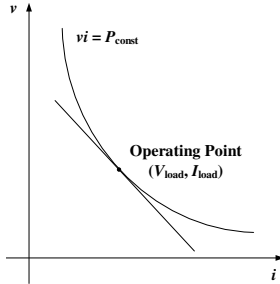

Fig. 2. Negative incremental impedance of CPL.

In order to solve the above problem caused by CPL, different approaches are proposed in the existing literature. The methods based on the modification of system configuration, achieved by either changing the hardware or implementing the required component virtually in the control diagram, are presented to enhance the system stability margin. In [28], a passive damping method is proposed, where the damper is classified into three categories: RC parallel damping, RL parallel damping and RL series damping. In [30], additional filters or the energy storage devices with huge rating are employed to solve the oscillation of DC bus voltage caused by CPLs. Meanwhile, the effect of load shedding is discussed to ensure stable operation. In [31], virtual resistance is employed to adjust the current flowing through the source and

DC link, which is useful for point-to-point system with one source and one load. Meanwhile, predictive control is involved to estimate the source voltage and current based on the measured DC-link voltage and system model, e.g. DC-link capacitance, source inductance, etc. In [32], virtual capacitance is implemented in the control system of load converter to reduce the size and weight of DC-link capacitor. The proposed method is realized by measuring the DC-link voltage and involving additional virtual capacitance loop. The load power reference is slightly adjusted by adding the output of the additional virtual capacitance loop into the original power reference. In [33], three technical approaches for stabilizing MVDC system with CPL are reviewed. The second approach, namely active damping approach, is realized by implementing virtual component. In particular, a control signal is obtained by measuring the load current and a virtual resistance is employed to generate a virtual voltage drop.

Linear or nonlinear feedback control methods have also been employed to enhance the stability of DC systems with CPLs. In [34] and [35], both nonlinear and linear approaches for stabilizing the system with CPL were proposed. The nonlinear stabilization is realized by using the stabilization law that is proportional to v_s^2, where v_s is the DC-link voltage, namely the input voltage of the CPL, and the linear stabilization is achieved by employing an additional compensating loop with small signal variable of DC-link voltage as the input. For these two papers, the configuration that is comprised of a DC source generated by a three-phase rectifier and a motor as CPL is employed. Both of the dynamics involved by the inverter and motor load are considered when designing the compensating loop. The proposed methods in these two papers are mainly designed for the system with single or multiple loads since the proposed approaches are implemented in the load inverters. These methods are suitable for the applications with multi-load configurations, e.g. DC systems on electric aircrafts and ships. In [33], two approaches based on state feedback are proposed for the converters in the generation side. For the first approach, the control signal is synthesized by using the feedback variables of load voltage and current, while for the second approach, two control functions are employed in the linearization-state-feedback-based control diagram. The first control function is used to compensate the system nonlinearities. After cancelling the nonlinearities, the original nonlinear system is changed to a linear system. The second control function is selected to realize a linear control on the derived linear system. This second approach is also shown in [19]. In [36], small-signal analysis is performed to discuss the stability issues of medium-voltage DC (MVDC) integrated power system. Based on the derived small-signal model, adaptive feedback control is employed in generation side control system. The proportional gains for voltage and current feedbacks are designed by considering the dynamic requirements of a common second-order system. In [30], passivity-based linear control and boundary control are employed to eliminate the oscillation behavior caused by

CPLs.

Besides the above methods to alleviate the instability issues in DC systems with CPLs, other effective methods are also proposed in the existing literature. In [17], sliding-mode control is used to improve the large signal stability and dynamic responses. In [37], a fault-tolerant multi-agent stabilizing system is proposed with the consideration of constrained optimization, where stabilizing agents are employed and different fault cases are considered to guarantee the feasibility of the approach. In [38], a DC power system with multiple CPLs are comprehensively studied. Both centralized Takagi-Sugeno method and decentralized agent-based method are developed to cope with the instability issues induced by CPLs. In [39], the system architectures and the impact of CPLs in multiple-converter-based vehicular electrical systems are discussed, and the pulse adjustment technology is employed to apply predefined duty cycle. Hence, a cost-effective approach is implemented to regulate the output voltage considering CPLs.

It should be noticed that, as aforementioned, the negative incremental impedance can be derived if neglecting the interaction between the CPLs and upstream converters [29]. By taking the dynamics and interactions of different interface converters into account, the analysis of the instability issues should be extended. In [29], the small-signal behavior of CPLs is studied. Meanwhile, it is revealed that the well-known negative impedance characteristic of CPL is an approximation if neglecting the dynamic interactions between converters.

III. MODELING AND STABILITY ANALYSIS OF DC MICROGRIDS WITH CPLS

A. Multi-Stage Configuration of DC Microgrids

A typical configuration of DC microgrids is shown in Fig. 3. Here, different types of renewable energy sources are considered. Without loss of generality, PVs and batteries are taken into account here.

The DC microgrid shown in Fig. 3 features multi-stage configuration. In the first stage, namely the source stage, in order to abstract the maximum available power, MPPT is employed for PVs. Meanwhile, the interface converter of battery is controlled to generate stable output voltage. Hence, in the source stage, the PV and battery are combined as a whole system to establish the local source bus with stable DC voltage. The second stage is comprised of interface converters which establish the local output bus and the transmission line. For the converters in this stage, their input side is connected to the local source bus. The input voltage is generated by the converters in the first stage. At the same time, their output sides are the local output buses. In order to build up the required voltage level at the local output bus and achieve proper power sharing among different interface converters, the converters in this stage is commonly controlled as voltage source with droop function as the outer control loop. Since stable input voltage of this stage is generated by the first stage, the interface converters in different stages can be easily decoupled and controlled. Finally, the third stage is the common load bus. Different local power units, which are constructed by the first and second stages, are collected at the PCC in the third stage. CPLs are connected at the common load bus in this stage. The proposed damping method is embedded in the generation side, i.e., in each distributed power generation unit. In particular, it is implemented in each interface converter in Stage II, as shown in the multi-stage configuration of DC microgrids in Fig. 3.

Different voltage levels can be used in DC microgrids. Here, a voltage level combination of 96 V, 380 V and 240 V is selected for the multi-stage DC microgrids as an example. Specifically, the PV and battery with rated output voltage of 96 V are selected in the first stage, and the output voltage, i.e. the source bus voltage, is controlled to 380 V. In the meantime, the output voltage of the second stage is selected as 240 V, i.e. the rated voltage of local output bus is 240 V. Since the voltage drop across the line impedance does not take a large percentage of the rated voltage, the rated voltage of PCC is also 240 V approximately. Since the converters in Stage I and Stage II are directly connected to form the distributed power generation units, they share the same local source bus, i.e. a capacitor is shared in the output side of the converters in Stage I and the input side of the converters in Stage II. Due to the rated voltage of each bus, different types of interface converters are selected. For PVs in the first stage, unidirectional boost converters are used as the interface. For batteries in the first stage, bidirectional converters are selected to achieve both of the charging and discharging functions. For the interface converters in the second stage, bidirectional buck converters are selected. Meanwhile, the proposed virtual-impedance-based stabilizers are connected at the output terminal of the buck converters, as shown in Fig. 4.

Considering the common configuration of DC microgrids, distributed control diagram should be developed. Hence, the distributed virtual-impedance-based stabilizer is proposed in this paper to achieve stable operation when CPLs exist in the system. It should be noticed that various types of configurations can be used for DC microgrids. Since the stabilization of DC microgrids with CPLs is the main research topic in this paper, only the typical and practical multi-stage configuration is used here.

B. Comprehensive Small-Signal Model of DC Microgrids with CPLs

In order to study the performance of the proposed virtual-impedance-based stabilizers, a comprehensive model of DC microgrids with CPLs should be derived first. As mentioned in the Section III-A, different types of interface converters are utilized in each stage. The detailed analysis of the overall system model is discussed as follows. Here, in order to make the derivation procedure clear, subscription '1' is used for PV unidirectional boost converter, subscription '2' is used for battery bidirectional boost converter, and subscription '3' is used for bidirectional buck converter between local source bus and local output bus.
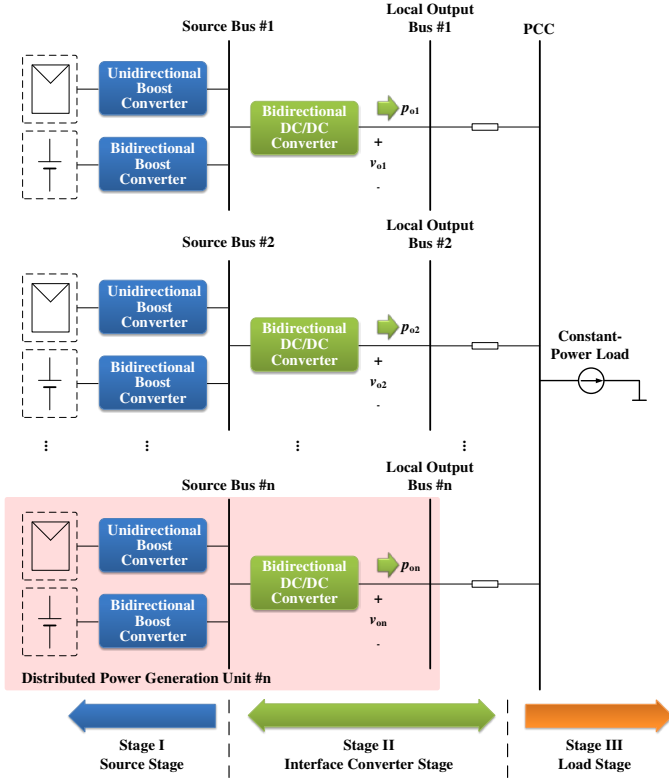
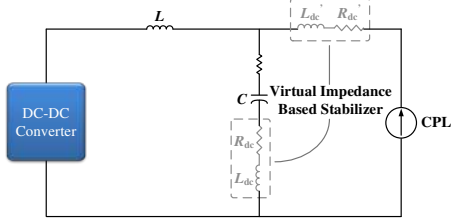Fig. 3. Multi-stage configuration of DC microgrids.

Fig. 4. Virtual-impedance-based stabilizers at the output terminal of interface converters.

For the unidirectional boost converters used for PVs, the converter topology is shown in Fig. 5 (a). In order to derive the detailed model of the converter, state-space averaging is employed [40]. When the switch turns on or off, the circuit topology is changed accordingly. If the switch turns on, it yields:

$$\begin{cases} \dfrac{di_{L1}}{dt} = \dfrac{1}{L_1} v_{s1} \\ \dfrac{dv_{C1}}{dt} = \dfrac{1}{C_1} i_{L1} - \dfrac{1}{C_1} i_{o1} \end{cases} \quad (2)$$

where i_{L1} is the inductor current, v_{C1} is the capacitor voltage, L_1 and C_1 are the inductance and capacitance respectively, v_{s1} is the input voltage, i_{o1} is the output current.

If the switch turns off, it is reached that:

$$\begin{cases} \dfrac{di_{L1}}{dt} = -\dfrac{r_{C1}}{L_1} i_{L1} - \dfrac{1}{L_1} v_{C1} + \dfrac{r_{C1}}{L_1} i_{o1} + \dfrac{1}{L_1} v_{s1} \\ \dfrac{dv_{C1}}{dt} = \dfrac{1}{C_1} i_{L1} - \dfrac{1}{C_1} i_{o1} \end{cases} \quad (3)$$

where r_{C1} is the parasitic resistance of the capacitor.

By using state-space averaging, the state-space function is derived as:

$$\begin{bmatrix} \dfrac{di_{L1}}{dt} \\ \dfrac{dv_{C1}}{dt} \end{bmatrix} = \begin{bmatrix} -\dfrac{r_{C1}}{L_1}(1-d_1) & -\dfrac{1}{L_1}(1-d_1) \\ \dfrac{1}{C_1}(1-d_1) & 0 \end{bmatrix} \cdot \begin{bmatrix} i_{L1} \\ v_{C1} \end{bmatrix} \\ + \begin{bmatrix} \dfrac{r_{C1}}{L_1}(1-d_1) \\ -\dfrac{1}{C_1} \end{bmatrix} \cdot i_{o1} + \begin{bmatrix} \dfrac{1}{L_1} \\ 0 \end{bmatrix} \cdot v_{s1} \quad (4)$$

where d_1 is the duty cycle for on-state of the switch.

Meanwhile, by analyzing the output side of the circuit, it yields that:

$$v_{o1} = [r_{C1}(1-d_1) \quad 1] \cdot \begin{bmatrix} i_{L1} \\ v_{C1} \end{bmatrix} - r_{C1} \cdot i_{o1} \quad (5)$$

where v_{o1} is the output voltage of the converter.

Based on the results in (4) and (5), the small-signal model is achieved as:

$$\begin{bmatrix} \dfrac{d\tilde{i}_{L1}}{dt} \\ \dfrac{d\tilde{v}_{C1}}{dt} \end{bmatrix} = \begin{bmatrix} -\dfrac{r_{C1}}{L_1}(1-D_1) & -\dfrac{1}{L_1}(1-D_1) \\ \dfrac{1}{C_1}(1-D_1) & 0 \end{bmatrix} \cdot \begin{bmatrix} \tilde{i}_{L1} \\ \tilde{v}_{C1} \end{bmatrix} \\ + \begin{bmatrix} \dfrac{1}{L_1}(r_{C1}I_{L1}+V_{C1}-r_{C1}I_{o1}) \\ -\dfrac{1}{C_1}I_{L1} \end{bmatrix} \cdot \tilde{d}_1 \\ + \begin{bmatrix} \dfrac{r_{C1}}{L_1}(1-D_1) \\ -\dfrac{1}{C_1} \end{bmatrix} \cdot \tilde{i}_{o1} + \begin{bmatrix} \dfrac{1}{L_1} \\ 0 \end{bmatrix} \cdot \tilde{v}_{s1} \quad (6)$$

$$\tilde{v}_{o1} = [r_{C1}(1-D_1) \quad 1] \cdot \begin{bmatrix} \tilde{i}_{L1} \\ \tilde{v}_{C1} \end{bmatrix} - r_{C1}I_{L1} \cdot \tilde{d}_1 - r_{C1} \cdot \tilde{i}_{o1} \quad (7)$$

where the variables showing in capital letter represent the steady-state values of duty cycle, inductor current, capacitor voltage and output current, the variables with '~' indicate the small-signal disturbance.

Let

$$A_1 = \begin{bmatrix} -\dfrac{r_{C1}}{L_1}(1-D_1) & -\dfrac{1}{L_1}(1-D_1) \\ \dfrac{1}{C_1}(1-D_1) & 0 \end{bmatrix},$$

$$B_{11} = \begin{bmatrix} \dfrac{1}{L_1}(r_{C1}I_{L1}+V_{C1}-r_{C1}I_{o1}) \\ -\dfrac{1}{C_1}I_{L1} \end{bmatrix}, B_{21} = \begin{bmatrix} \dfrac{r_{C1}}{L_1}(1-D_1) \\ -\dfrac{1}{C_1} \end{bmatrix}, B_{31} = \begin{bmatrix} \dfrac{1}{L_1} \\ 0 \end{bmatrix}, \quad (8)$$

$$C_1 = [r_{C1}(1-D_1) \quad 1], D_{11} = -r_{C1}I_{L1}, D_{21} = -r_{C1}$$

Hence, the small-signal model of the state-space function in (6) and (7) can be simplified as:

$$\begin{bmatrix} \dfrac{d\tilde{i}_{L1}}{dt} \\ \dfrac{d\tilde{v}_{C1}}{dt} \end{bmatrix} = A_1 \cdot \begin{bmatrix} \tilde{i}_{L1} \\ \tilde{v}_{C1} \end{bmatrix} + B_{11} \cdot \tilde{d}_1 + B_{21} \cdot \tilde{i}_{o1} + B_{31} \cdot \tilde{v}_{s1} \quad (9)$$

$$\tilde{v}_{o1} = C_1 \cdot \begin{bmatrix} \tilde{i}_{L1} \\ \tilde{v}_{C1} \end{bmatrix} + D_{11} \cdot \tilde{d}_1 + D_{21} \cdot \tilde{i}_{o1} \qquad (10)$$

By transferring the linear small-signal model in (9) and (10) into frequency domain and combining the results, it is derived that:

$$\begin{aligned} \tilde{v}_{o1}(s) = &[C_1(sI - A_1)^{-1}B_{11} + D_{11}] \cdot \tilde{d}_1(s) \\ &+ C_1(sI - A_1)^{-1}B_{31} \cdot \tilde{v}_{s1}(s) \\ &- [-C_1(sI - A_1)^{-1}B_{21} - D_{21}] \cdot \tilde{i}_{o1}(s) \end{aligned} \qquad (11)$$
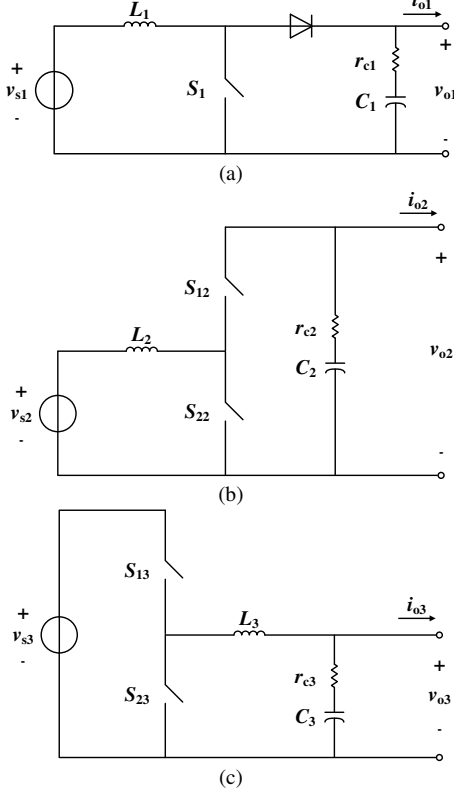

(a)

(b)

(c)

Fig. 5. Topologies of interface converters in different stages.
(a) Unidirectional boost converter. (b) Bidirectional boost converter. (c) Bidirectional buck converter.

Since the interface converter for PV is used to reach MPPT and does not need to establish the voltage of source bus, a basic control diagram shown in Fig. 6 (a) is used. Hence, the small-signal model of the control diagram in frequency domain is achieved:

$$(\tilde{v}_{s1}^*(s) - \tilde{v}_{s1}(s)) \cdot G_{pi1}G_d = \tilde{d}_1(s) \qquad (12)$$

where G_d represents the unit PWM delay.

It should be noted that the impact of MPPT on PV is represented by the perturbation in the reference value of the PV output voltage $\tilde{v}_{s1}^*$.

By analyzing the simultaneous equations of (11) and (12), it yields:

$$\begin{aligned} \tilde{v}_{o1}(s) = &[C_1(sI - A_1)^{-1}B_{11} + D_{11}] \cdot G_{pi1}G_d \cdot \tilde{v}_{s1}^*(s) \\ &+ \{C_1(sI - A_1)^{-1}B_{31} - [C_1(sI - A_1)^{-1}B_{11} + D_{11}] \cdot G_{pi1}G_d\} \cdot \tilde{v}_{s1}(s) \\ &- [-C_1(sI - A_1)^{-1}B_{21} - D_{21}] \cdot \tilde{i}_{o1}(s) \end{aligned} \qquad (13)$$

Let

$$\begin{aligned} G_{11} &= [C_1(sI - A_1)^{-1}B_{11} + D_{11}] \cdot G_{pi1}G_d \\ G_{21} &= C_1(sI - A_1)^{-1}B_{31} - C_1(sI - A_1)^{-1}B_{11}G_{pi1}G_d - D_{11}G_{pi1}G_d \\ Z_{o1} &= -C_1(sI - A_1)^{-1}B_{21} - D_{21} \end{aligned} \qquad (14)$$

Therefore, (13) can be simplified as:

$$\tilde{v}_{o1}(s) = [G_{11} \cdot \tilde{v}_{s1}^*(s) + G_{21} \cdot \tilde{v}_{s1}(s)] - Z_{o1} \cdot \tilde{i}_{o1}(s) \qquad (15)$$

It is seen from (15) that in the small-signal model, the output voltage of the converter can be represented by two parts. The first part is the controlled voltage source determined by the reference and measured value of the input voltage of the converter, i.e. the output voltage of PV panel; the second part is the output impedance. Hence, the dynamics involved by MPPT that is represented by $\tilde{v}_{s1}^*$, input voltage and output current are all taken into account.
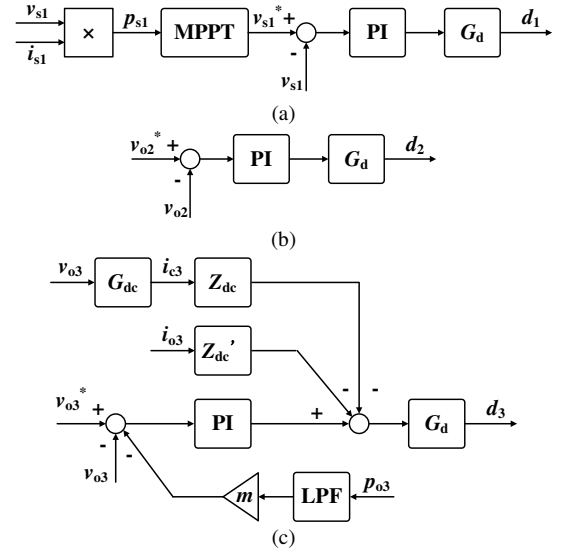

(a)

(b)

(c)

Fig. 6. Control diagram of different interface converters.
(a) Control diagram of unidirectional boost converter. (b) Control diagram of bidirectional boost converter. (c) Control diagram of bidirectional buck converter.

The above discussion is for the modeling of unidirectional boost converter that is used for PV. For the bidirectional boost converter used for battery, the analysis is the same as that for PV converter. The basic topology of bidirectional boost converter is shown in Fig. 5 (b). In order to avoid repetition, no detailed procedures are shown below. It can be finally derived that:

$$\begin{aligned} \tilde{v}_{o2}(s) = &[C_2(sI - A_2)^{-1}B_{12} + D_{12}] \cdot \tilde{d}_2(s) \\ &+ C_2(sI - A_2)^{-1}B_{32} \cdot \tilde{v}_{s2}(s) \\ &- [-C_2(sI - A_2)^{-1}B_{22} - D_{22}] \cdot \tilde{i}_{o2}(s) \end{aligned} \qquad (16)$$

where A_2, B_{12}, B_{22}, B_{32}, C_2, D_{12} and D_{22} follow the similar expressions compared to A_1, B_{11}, B_{21}, B_{31}, C_1, D_{11} and D_{21}. Only the subscriptions should be changed.

The battery converter is used for establishing the source bus, so its basic control diagram is shown in Fig. 6 (b). Based on this control diagram, the small-signal model is achieved:

$$-\tilde{v}_{o2}(s) \cdot G_{pi2}G_d = \tilde{d}_2(s) \qquad (17)$$

Since the battery converter is used to establish the stable source bus voltage, its reference value is set to the constant

value of 380 V. Therefore, no dynamics of the reference value is considered in (17).

By solving the simultaneous equations of (16) and (17), it yields:

$$\tilde{v}_{o2}(s) = G_{12} \cdot \tilde{v}_s(s) - Z_{o2} \cdot \tilde{i}_o(s) \qquad (18)$$

where

$$G_{12} = [1 + G_{pi2}G_d C_2(sI - A_2)^{-1}B_{12} + G_{pi2}G_d D_{12}]^{-1}$$
$$\cdot C_2(sI - A_2)^{-1}B_{32}$$
$$Z_{o2} = [1 + G_{pi2}G_d C_2(sI - A_2)^{-1}B_{12} + G_{pi2}G_d D_{12}]^{-1}$$
$$\cdot [-C_2(sI - A_2)^{-1}B_{22} - D_{22}]$$

It can be seen from (18) that, similar to the unidirectional boost converter for PV, the small-signal model of the bidirectional boost converter can be also represented by the Thevenin equivalent model with the voltage source of $G_{12} \cdot \tilde{v}_s(s)$ and output impedance of Z_{o2}. The dynamics involved by both of the source voltage and output current is considered.

For the buck converters between the local source bus (380 V) and local output bus (240 V), the basic topology is shown in Fig. 5 (c). By using the similar procedure above, it is derived that:

$$\tilde{v}_{o3}(s) = C_3(sI - A_3)^{-1}B_{13} \cdot \tilde{d}_3(s)$$
$$+ C_3(sI - A_3)^{-1}B_{33} \cdot \tilde{v}_{s3}(s) \qquad (19)$$
$$- [-C_3(sI - A_3)^{-1}B_{23} - D_{23}] \cdot \tilde{i}_{o3}(s)$$

where

$$A_3 = \begin{bmatrix} -\dfrac{r_{C3}}{L_3} & -\dfrac{1}{L_3} \\ \dfrac{1}{C_3} & 0 \end{bmatrix},$$

$$B_{13} = \begin{bmatrix} -\dfrac{1}{L_3}V_{s3} \\ 0 \end{bmatrix}, B_{23} = \begin{bmatrix} \dfrac{r_{C3}}{L_3} \\ -\dfrac{1}{C_3} \end{bmatrix}, B_{33} = \begin{bmatrix} \dfrac{1}{L_3}(1-D_3) \\ 0 \end{bmatrix},$$

$$C_3 = [r_{C3} \quad 1], D_{23} = -r_{C3}$$

Considering the control diagram in Fig. 6 (c), it is reached:

$$d_3(s) = \{[v_{o3}^*(s) - v_{o3}(s) - m \cdot G_{lpf} \cdot p_{o3}(s)] \cdot G_{pi3} \qquad (20)$$
$$- v_{o3}(s) \cdot G_{dc}Z_{dc} - i_{o3}(s) \cdot Z_{dc}'\} \cdot G_d$$

where m is the droop coefficient, G_{lpf} is the transfer function of low-pass filter, p_{o3} is the output power.

Droop control is considered in the control diagram. Meanwhile, the virtual-impedance-based stabilizers are employed, which are shown as Z_{dc} and Z_{dc}' in (20). Here, Z_{dc} and Z_{dc}' are expressed as:

$$Z_{dc} = s \cdot L_{dc} + R_{dc} \qquad (21)$$

$$Z_{dc}' = s \cdot L_{dc}' + R_{dc}' \qquad (22)$$

where L_{dc}, R_{dc}, L_{dc}' and R_{dc}' are the virtual inductance and resistance respectively.

For the output power, it satisfies the expression below:

$$p_{o3} = v_{o3} \cdot i_{o3} \qquad (23)$$

Hence, the small-signal expression of (23) can be shown as:

$$\tilde{p}_{o3} = V_{o3} \cdot \tilde{i}_{o3} + I_{o3} \cdot \tilde{v}_{o3} \qquad (24)$$

By transferring (24) into frequency domain and substituting the result into (20), it is obtained:

$$\tilde{d}_3(s) = -[(1 + mG_{lpf}I_{o3})G_{pi3} + G_{dc}Z_{dc}]G_d \cdot \tilde{v}_{o3}(s) \qquad (25)$$
$$- (mG_{lpf}V_{o3}G_{pi3} + Z_{dc}')G_d \cdot \tilde{i}_{o3}(s)$$

By substituting (25) into (19), it yields:

$$\tilde{v}_{o3}(s) = G_{13} \cdot \tilde{v}_{s3}(s) - Z_{o3} \cdot \tilde{i}_{o3}(s) \qquad (26)$$

where

$$G_{13} = \{1 + C_3 G_d(sI - A_3)^{-1}B_{13}[(1 + mG_{lpf}I_{o3})G_{pi3} + G_{dc}Z_{dc}]\}^{-1}$$
$$\cdot C_3(sI - A_3)^{-1}B_{33}$$
$$Z_{o3} = \{1 + C_3 G_d(sI - A_3)^{-1}B_{13}[(1 + mG_{lpf}I_{o3})G_{pi3} + G_{dc}Z_{dc}]\}^{-1}$$
$$\cdot [C_3 G_d(sI - A_3)^{-1}B_{13}(mG_{lpf}V_{o3}G_{pi3} + Z_{dc}') - C_3(sI - A_3)^{-1}B_{23} - D_{23}]$$

Therefore, the Thevenin equivalent model of the interface converters between the local source bus and local output bus is also derived considering droop control and the proposed virtual-impedance-based stabilizers. The dynamics of the converter input voltage and output current are both considered in the derived small-signal model.

For the POL converter, a buck converter with a resistor as its load is selected as an example to represent the CPL. Conventional proportional-integral (PI) controller is used to regulate the output voltage of this POL converter. As suggested in [29], the small-signal dynamics can be represented by the closed-loop input impedance of the POL converter, as shown in (27), which is a more accurate way compared to the traditional approximation by using pure negative resistance.

$$Z_L = \frac{R_L C_L L_L \cdot s^3 + L_L \cdot s^2 + R_L(1 + K_{pL}V_{inL}) \cdot s + R_L K_{iL}V_{inL}}{R_L C_L D_L^2 \cdot s^2 + (D_L^2 - K_{pL}D_L^2 V_{inL}) \cdot s - K_{iL}D_L^2 V_{inL}} \qquad (27)$$

where Z_L and R_L are the closed-loop input impedance and load resistance of the POL converter, C_L and L_L are the capacitance and inductance of the output filter, V_{inL} is the steady-state input voltage of the POL converter, K_{pL} and K_{iL} are the proportional and integral terms of the PI controller, D_L is the duty cycle in steady state.

By summarizing the results in (15), (18), (26) and (27), the small-signal models of the multi-stage configuration of DC microgrids is obtained, as shown in Fig. 7. Meanwhile, the transmission line that is connected to the common load bus with aggregated CPLs is also taken into account in the derived model.

C. Stability Analysis

Based on the comprehensive small-signal model derived in Section III-B, stability analysis can be accomplished by using the criteria of impedance matching.

The small-signal model in Fig. 7 can be divided into two sections, i.e. the local source section and common load section. The local source section includes Stage I and II, while the common load section includes Stage III. In order to get the stable system, the dominant poles of the following small-signal expression in (28) should all locate in the stable region.

$$p = (1 + \frac{Z_s}{Z_L})^{-1} \qquad (28)$$

where Z_s is the small-signal output impedance of the source.

For each distributed power unit, it can be derived from the detailed small-signal model in Fig. 7 that:

$$\tilde{v}_{o3}(s) = \frac{G_{13}(G_{11}Z_{o2}\tilde{v}_{s1}^*(s) + G_{21}Z_{o2}\tilde{v}_{s1}(s) + G_{12}Z_{o1}\tilde{v}_{s2}(s))}{Z_{o1} + Z_{o2}} \quad (29)$$
$$-\frac{Z_{o1}Z_{o2}G_{13}^2 + Z_{o1}Z_o + Z_{o2}Z_o}{Z_{o1} + Z_{o2}} \cdot \tilde{i}_{o3}(s)$$

Hence, the equivalent output impedance for each local power stage is derived as:

$$Z_{si} = \frac{Z_{o1}Z_{o2}G_{13}^2 + Z_{o1}Z_o + Z_{o2}Z_o}{Z_{o1} + Z_{o2}} \quad (30)$$

where Z_{si} is the source-side output impedance for distributed power unit #i.

By taking the transmission lines into account, the source-side impedance is obtained:

$$Z_s = (Z_{s1} + Z_{\text{line1}}) / /(Z_{s2} + Z_{\text{line2}}) / / \cdots / /(Z_{sn} + Z_{\text{linen}}) \quad (31)$$

Meanwhile, the load-side input impedance can be represented by using the impedance calculated in (27). By substituting (27) and (31) into (28), the system stability can be evaluated by testing the positions of the dominant poles of polynomial p.
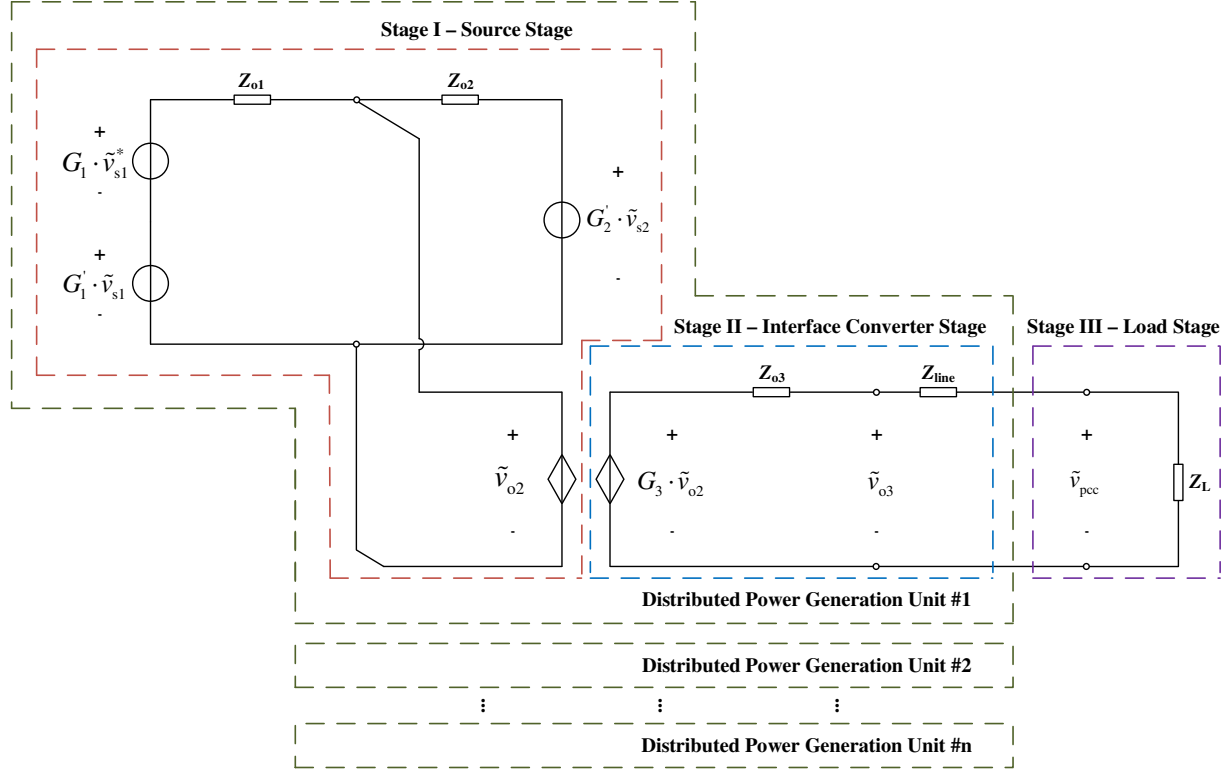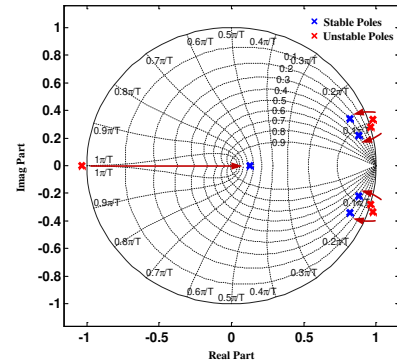

Fig. 7. Small-signal model of multi-stage configuration for DC microgrids.

As shown in Fig. 8, when the virtual-impedance-based stabilizers are not activated, instable dominant poles can be found in z domain. They are -1.04, 0.98 ± j 0.34 and 0.96 ± j 0.28, respectively. When the virtual stabilizers are activated, the original instable dominant poles are forced to move into the unit circle. Hence, the system stability is guaranteed. In particular, the above instable poles are changed to 0.13, 0.82 ± j 0.34 and 0.88 ± j 0.22, respectively. Here, R_{dc}, L_{dc}, R_{dc}' and L_{dc}' are selected as 0.6 Ω, 4 mH, 0.4 Ω and 1 mH.

The effectiveness of the proposed stabilizer can be also tested by changing the value of the virtual impedances, as shown in Fig. 9. For example, in Fig. 9 (a), when R_{dc}, R_{dc}' and L_{dc}' are fixed to 0.6 Ω, 0.4 Ω and 1 mH respectively, and L_{dc} changes from 500 μH to 6 mH, the trajectory of dominant poles of the polynomial p is shown in Fig. 9 (a). It can be seen that dominant pole V keeps at the same position, while the other two pairs of dominant poles move towards the stable region. It is seen that by selecting proper virtual impedances, the instable poles can be moved to the stable region, so the system stability can be ensured.

Fig. 8. Dominant poles of polynomial p w/o virtual-impedance-based stabilizers.

It should be noticed that the selection of virtual resistance and inductance is determined by evaluating system stability. The selected virtual impedance should ensure the stable operation of the whole system, i.e. all the dominant poles are located in the unit cycle of z domain.
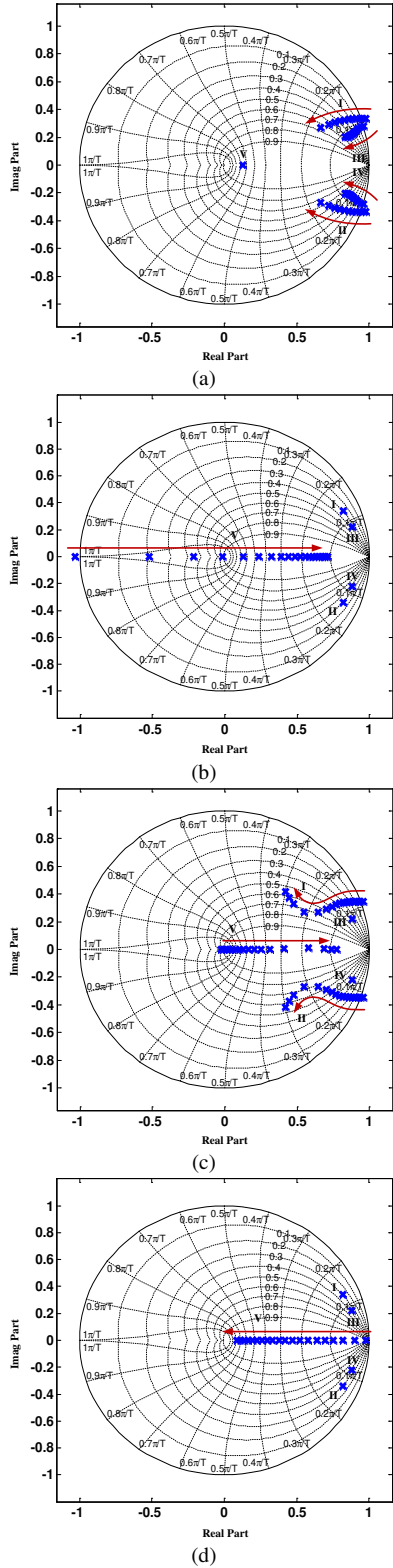
(a)

(b)

(c)

(d)

Fig. 9. Trajectory of polynomial p with changing parameters of virtual impedance.
(a) $R_{dc} = 0.6\ \Omega$, $L_{dc}^{'} = 1$ mH , $R_{dc}^{'} = 0.4\ \Omega$, L_{dc} changes from 500 μH to 6 mH.
(b) $L_{dc} = 4$ mH, $L_{dc}^{'} = 1$ mH, $R_{dc}^{'} = 0.4\ \Omega$, R_{dc} changes from 0.02 Ω to 1 Ω.
(c) $L_{dc} = 4$ mH, $R_{dc} = 0.6\ \Omega$, $R_{dc}^{'} = 0.4\ \Omega$, $L_{dc}^{'}$ changes from 200 μH to 3 mH.
(d) $L_{dc} = 4$ mH, $R_{dc} = 0.6\ \Omega$, $L_{dc}^{'} = 1$ mH, $R_{dc}^{'}$ changes from 0.02 Ω to 1 Ω.
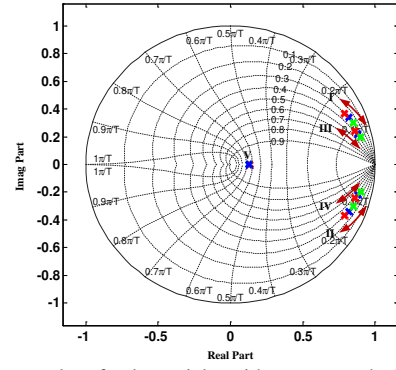
Fig. 10. Dominant poles of polynomial p with parameter deviation.

TABLE I
SYSTEM PARAMETERS

Item	Value	Unit
Rated PV Output Voltage	96	V
Input Inductor L_1	400	μH
Output Capacitor C_1	400	μF
Parasitic Resistor R_1	0.002	Ω
Rated Battery Output Voltage	96	V
Input Inductor L_2	400	μH
Output Capacitor C_2	400	μF
Parasitic Resistor R_2	0.002	Ω
Local Source Bus Voltage	380	V
Common Load Bus Voltage	200 ~ 280	V
Output Inductor L_3	600	μH
Output Capacitor C_3	300	μF
Parasitic Resistor R_3	0.002	Ω
Load Power	1 ~ 4	kW

Considering the inevitable parameter deviation of different power stages in real DC microgrids, the parameter sensibility of the proposed stabilizer is also tested. As shown in Fig. 10, a ±20% error of the inductance and capacitance of the output filter in the power stage is involved. It is seen that with parameter deviation, although the location of the dominant poles changes, they still locate in the stable region since the stabilizer is activated.

IV. SIMULATION VALIDATION

Simulation tests based on MATLAB/Simulink are performed to validate the virtual-impedance-based stabilizers. The configuration shown in Fig. 3 that is comprised of three distributed power units is studied in the simulation model. The system parameters are listed in Table I.

Case I: Testing of Distributed Power Unit with Combined Sources with PV and Battery

Since the main research topic in this study is the elimination of instability issues induced by CPLs, only basic control diagram is used for PV and battery. For PV, as aforementioned, unidirectional boost converter is used. It works at MPPT mode to track the maximum power from the solar panel. The solar power, PV output power and their difference are shown in Fig. 11. The controller for MPPT starts tracking the changing solar power after the initial period. It can be seen that the output power of PV panel follows the changing trend of the input solar power. Meanwhile, the output voltage of PV panel is

shown in Fig. 12. It can be seen that the output voltage of PV panel is changed to track the solar power after the initial period.

Different from the PV converter, the bidirectional boost converter for battery is used to establish the local source bus with a voltage control loop. Hence, the injected power from the PV converter to the source bus can be regarded as a disturbance. The source bus voltage is controlled to 380 V as required with changing injected solar power, as shown in voltage waveform in Fig. 13.

Meanwhile, by using the bidirectional buck converter, the local output bus of the distributed power unit is established. The local output bus is controlled to the rated value of 240 V, as shown in Fig. 14. Since single distributed power stage is tested first, no droop control is utilized. Hence, there is no deviation at the local output bus.

Case II: Activation and Deactivation of the Stabilizer

After testing the basic function of distributed power stage, the effectiveness of the proposed virtual-impedance-based stabilizer is verified.

The performance of the stabilizer is shown in the waveform of output power. As shown in Fig. 15 (a), before $t = 5$ s, the stabilizer is not activated. Hence, severe instability issue can be found in the output power waveform of unit #1. At $t = 5$ s, the stabilizer is activated, and the output power becomes 1 kW after a short dynamic process. It should be also noted that CPL of 3 kW is connected to the common load bus. By using droop control, the load power is equally shared by three power stages.

As shown in Fig. 15 (b), at $t = 40$ s, the stabilizer is deactivated. Due to the influence of CPL, the system becomes instable.

Case III: Changing of Operating Points

The stability analysis is performed based on small-signal model in Section III. In order to test the proposed stabilizers, it is necessary to verify the performance with different operating points.
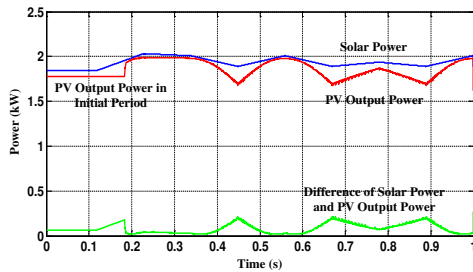
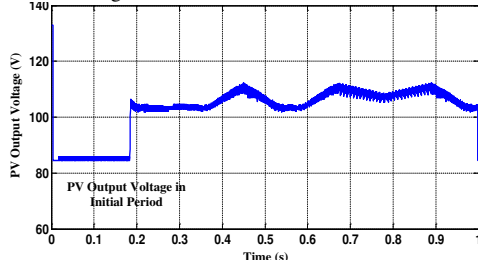
Fig. 11. Power tracking of solar converter.
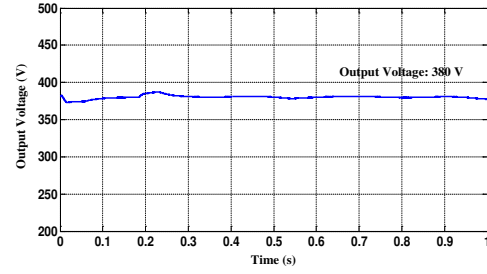

Fig. 12. Output voltage of PV panel.

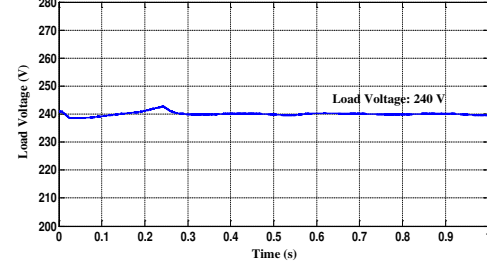Fig. 13. Voltage of local source bus.
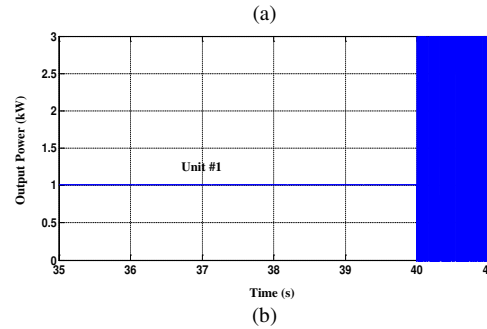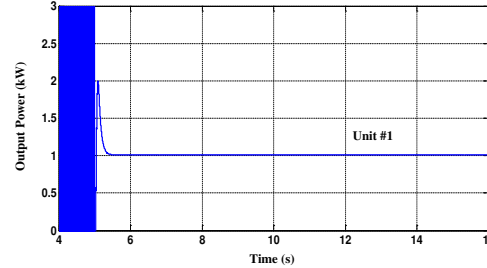

Fig. 14. Voltage of local output bus.

(a)

(b)

Fig. 15. Activation and deactivation of virtual-impedance-based stabilizer. (a) Output power of unit #1 with stabilizer activation. (b) Output power of unit #1 with stabilizer deactivation.

Continuous load step-up change occurs at the common load bus. In particular, the CPL changes following the sequence of 1.2 kW, 1.8 kW, 2.4 kW, 3 kW and 3.6 kW. By using the proposed stabilizer and droop control, as shown in Fig. 16 (a), the output power of unit #1 changes following the sequence of 0.4 kW, 0.6 kW, 0.8 kW, 1 kW and 1.2 kW, which are all one-third of the related load power. Meanwhile, stable operation is guaranteed in the whole process by using virtual-impedance-based stabilizer.

Furthermore, the performance of the system with continuous voltage reference step-up change is also tested. In particular, the rated voltage of the local output bus is set to change following the sequence of 200 V, 220 V, 240 V, 260 V and 280 V. It is seen in Fig. 16 (b) that with the proposed stabilizer, stable operation is maintained in the whole process. It should be noted that the output voltage of the local bus is slightly lower than its rated value. It is because that droop control is used in the control.

Similar to the above conditions, the results of load power and voltage step-down change are shown in Fig. 16 (c) and (d). In particular, in Fig. 16 (c), the load power decreases following the sequence of 3.6 kW, 3 kW, 2.4 kW, 1.8 kW and 1.2 kW. Hence, considering equal load power sharing among three units, the output power of unit #1 follows the sequence of 1.2 kW, 1 kW, 0.8 kW, 0.6 kW and 0.4 kW. In Fig. 16 (d), the voltage reference changes following the sequence of 280 V, 260 V, 240 V, 220 V and 200 V.

Case IV: Plug-and-Play of Distributed Power Generation Units

In order to further test the dynamic performance of the system with the proposed stabilizer, plug-and-play of distributed power generation units is studied.

As shown in Fig. 17 (a) – (c), three distributed power units are connected to the load bus sequentially. Before $t = 20$ s, only power unit #1 is started. Hence, all the CPL of 2 kW is supplied by unit #1. At $t = 20$ s, unit #2 is started. Hence, the load power is shared between these two power stages. The output power of each unit, i.e. unit #1 and #2, is 1 kW. At $t = 40$ s, unit #3 is started. Therefore, the load power of 2 kW is shared among three modules. Each of them delivers 0.67 kW output power. During the whole process of dynamic connection, the system stability is ensured by using the proposed stabilizer.

As shown in Fig. 18 (a) – (c), three distributed power units are disconnected sequentially. Before $t = 20$ s, three units work together to feed the CPL of 2 kW. Each one delivers 0.67 kW output power. At $t = 20$ s, unit #2 is disconnected. Hence, each of unit #1 and #3 delivers 1 kW. At $t = 40$ s, unit #3 is disconnected. The load power of 2 kW is only supplied by unit #1. As same as the results for dynamic connection, during the whole process of dynamic disconnection, the system stability is guaranteed by using the proposed stabilizer.

It should be noticed that some over-shoots/under-shoots in the output power waveforms can be found during connection, while the over-shoots/under-shoots cannot be observed obviously in the waveforms for disconnection process. The reason for this can be summarized below. Since the output voltage of each distributed power generation unit is controlled, each unit behaves as a voltage source. This is the nature of the difference of dynamic process when connecting or disconnecting each unit. It is known that for a voltage source, the dynamic performance when disconnecting from a voltage bus is better than the case when connecting it to a voltage bus. During connecting process, the existing voltage bus can be regarded as another voltage source. Since the generation unit to be connected is also a voltage source, the over-shoots/under-shoots are much easier to be found due to the slight voltage difference of these two voltage sources and the rather low connecting impedance between them. However, during disconnecting process, since no inrush current is generated, no obvious over-shoots/under-shoots are stimulated.

Case V: Testing of Parameter Deviation

In order to test the performance of the stabilizer with parameter deviation, the inductance and capacitance of the output filter in the interface converters between local source bus and local output bus is changed. In particular, the inductance and capacitance for the converter in unit #2 are changed to have a -20% error, while the inductance and capacitance for the converter in unit #3 are changed to have a +20% error. The parameters of the filter for unit #1 keep the original value.

Meanwhile, in order to further test the parameter deviation induced by the control diagram, the droop coefficients for unit #1, #2 and #3 are changed from equal values to those following the relationship of 1:2:3. Previously, the droop coefficients for each unit are the same.

The above parameter differences are activated at $t = 30$ s. By involving the above differences in the main power circuit and control diagram, the output power of each power module is shown in Fig. 19. It is seen that stable operation is also ensured with different parameters. Meanwhile, by using proportional droop coefficients, the output power of each module follows the inverse proportion of droop coefficients, which is 3:2:1. Although parameter deviations are involved for the passive components in the output filter, the output power of each unit also follows the desired value that is inversely proportional to the droop coefficients.
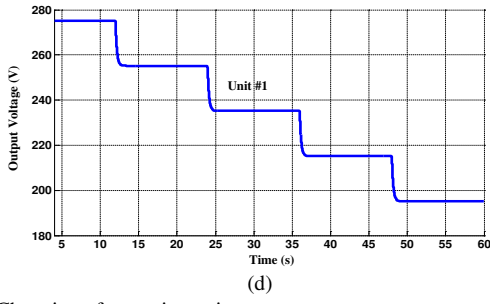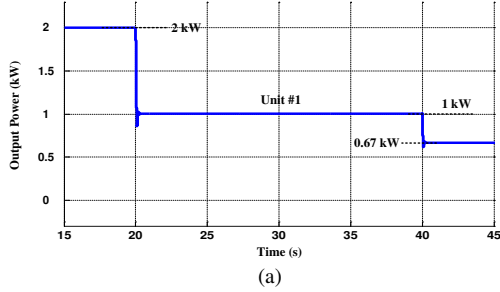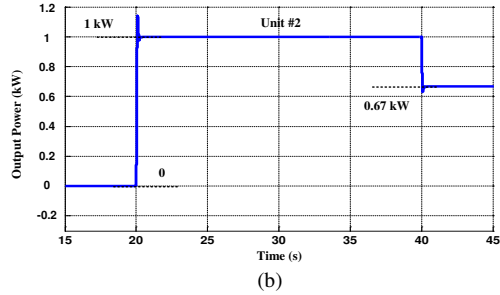

(a)

(b)
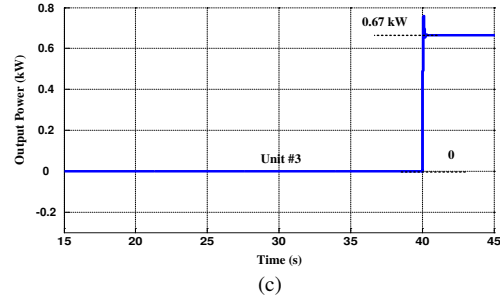

(c)

(d)
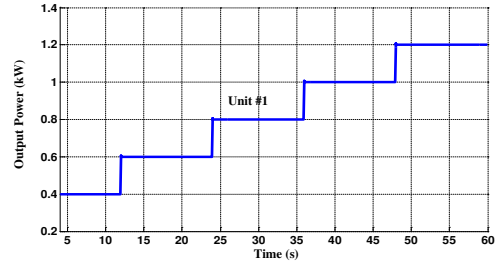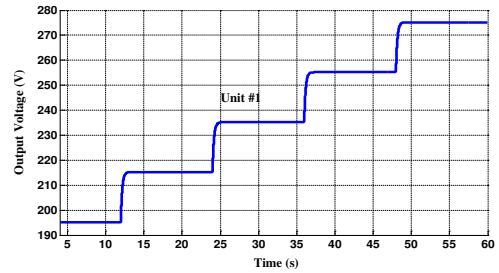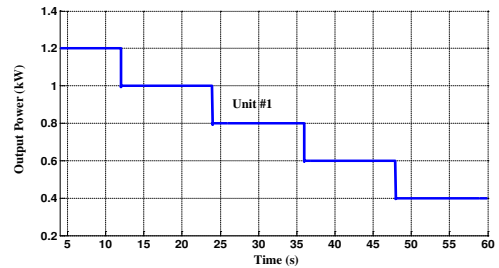
Fig. 16. Changing of operating point.
(a) Output power of unit #1 with load power step-up. (b) Output power of unit #1 with voltage reference step-up. (c) Output power of unit #1 with load power step-down. (d) Output power of unit #1 with voltage reference step-down.
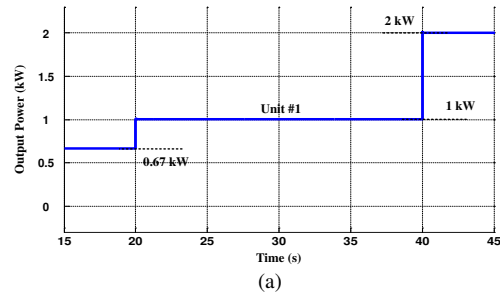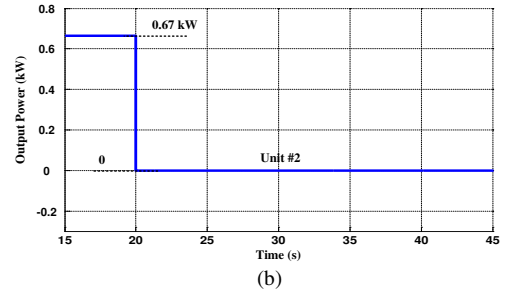

(a)

(b)

(c)

Fig. 17. Dynamic connection of each unit with virtual-impedance-based stabilizer activated.
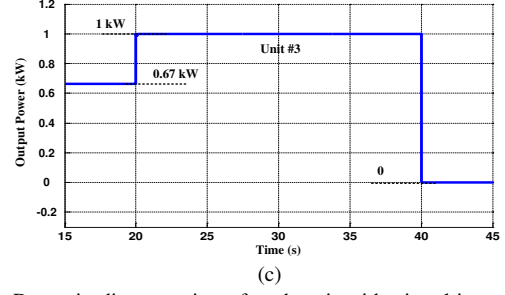(a) Output power of unit #1. (b) Output power of unit #2. (c) Output power of unit #3.

(a)

(b)

(c)

Fig. 18. Dynamic disconnection of each unit with virtual-impedance-based stabilizer activated.
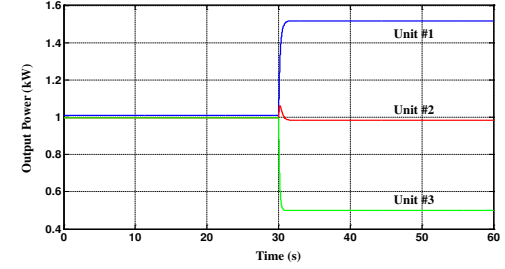(a) Output power of unit #1. (b) Output power of unit #2. (c) Output power of unit #3.

Fig. 19. Output power of three units with parameter deviation in the output filter and different droop coefficients.

V. CONCLUSION

In this paper, virtual-impedance-based stabilizers are proposed to enhance the stability of DC microgrids with CPLs. A comprehensive small-signal model of multi-stage DC microgrid is derived. Based on this model, the system stability considering the impact of CPL and the proposed stabilizer is studied. By using the criteria of impedance matching, it is demonstrated that the instable poles induced CPLs are forced to move into the stable region with properly designed stabilizers. Hence, the system stability can be guaranteed.

REFERENCES

[1] R. Lasseter, A. Akhil, C. Marnay, J. Stevens, et al, "The certs microgrid concept - white paper on integration of distributed energy resources," *Technical Report*, U.S. Department of Energy, 2002.

[2] A. A. A. Radwan and Y. A. R. I. Mohamed, "Modeling, analysis, and stabilization of converter-fed AC microgrids with high penetration of converter-interfaced loads," *IEEE Trans. Smart Grid*, vol. 3, no. 3, pp. 1213-1225, 2012.

[3] D. Dong, T. Thacker, I. Cvetkovic, R. Burgos, D. Boroyevich, et al, "Modes of operation and system-level control of single-phase bidirectional PWM converter for microgrid systems," *IEEE Trans. Smart Grid*, vol. 3, no. 1, pp. 93-104, 2012.

[4] Y. W. Li and C. N. Kao, "An accurate power control strategy for power-electronics-interfaced distributed generation units operating in a low-voltage multibus microgrid," *IEEE Trans. Power Electron.*, vol. 24, no. 12, pp. 2977-2988, 2009.

[5] Q. C. Zhong, "Robust droop controller for accurate proportional load sharing among inverters operated in parallel," *IEEE Trans. Ind. Electron.*, vol. 60, no. 4, pp. 1281-1290, 2013.

[6] N. Pogaku, M. Prodanović and T. C. Green, "Modeling, analysis and testing of autonomous operation of an inverter-based microgrid," *IEEE Trans. Power Electron.*, vol. 22, no. 2, pp. 613-625, 2007.

[7] J. M. Guerrero, M. Chandorkar, T. L. Lee and P. C. Loh, "Advanced control architectures for intelligent microgrids – part I: decentralized and hierarchical control," *IEEE Trans. Ind. Electron.*, vol. 60, no. 4, pp. 1254-1262, 2013.

[8] H. Valderrama-Blavi, J. M. Bosque, F. Guinjoan, L. Marroyo and L. Martínez-Salamero, "Power adaptor device for domestic dc microgrids based on commercial MPPT inverter," *IEEE Trans. Ind. Electron.*, vol. 60, no. 3, pp. 1191-1203, 2013.

[9] A. Pratt, P. Kumar and T. V. Aldridge, "Evaluation of 400V DC distribution in telco and data centers to improve energy efficiency," *in Proc. of INTELEC*, pp. 32-39, 2007.

[10] H. Kakigano, M. Nomura and T. Ise, "Loss evaluation of dc distribution for residential houses compared with ac system," *in Proc. of IPEC*, pp. 480-486, 2010.

[11] T. F. Wu, K. H. Sun, C. L. Kuo and C. H. Chang, "Predictive current controlled 5-kW single-phase bidirectional inverter with wide inductance variation for dc-microgrid applications," *IEEE Trans. Power Electron.*, vol. 25, no. 12, pp. 3076-3084, 2010.

[12] D. Dong, I. Cvetkovic, D. Boroyevich, W. Zhang, R. Wang, et al, "Grid-interface bi-directional converter for residential DC distribution systems – part one: high-density two-stage topology," *IEEE Trans. Power Electron.*, vol. 28, no. 4, pp. 1655-1666, 2013.

[13] J. M. Guerrero, J. C. Vasquez, J. Matas, G. G. De Vicuña and M. Castilla, "Hierarchical control of droop-controlled AC and DC microgrids - a general approach toward standardization," *IEEE Trans. Ind. Electron.*, vol. 58, no. 1, pp. 158-172, 2011.

[14] X. Lu, J. M. Guerrero and K. Sun, "An improved control method for dc microgrids based on low bandwidth communication with DC bus voltage restoration and enhanced current sharing accuracy," *IEEE Trans. Power Electron.*, vol. 29, no. 4, pp. 1800-1812, 2014.

[15] X. Lu, K. Sun, J. M. Guerrero, J. C. Vasquez and L. Huang, "State-of-charge balance using adaptive droop control for distributed energy storage systems in DC microgrid applications," *IEEE Trans. Ind. Electron.*, vol. 61, no. 6, pp. 2804-2815, 2014.

[16] X. Lu, K. Sun, J. M. Guerrero, J. C. Vasquez and L. Huang, "Double-quadrant state-of-charge-based droop control method for distributed energy storage systems in autonomous DC microgrids," *IEEE Trans. Smart Grid*, vol. 6, no. 1, pp. 147-157, 2015.

[17] A. Emadi, B. Fahimi, and M. Ehsani, "On the concept of negative impedance instability in advanced aircraft power systems with constant power loads," *Soc. Automotive Eng. (SAE) J.,* vol. 1, no. 1, 1999.

[18] M. Gries, O. Wasynczuk, B. Selby and P. T. Lamm, "Designing for large-displacement stability in aircraft power systems," *Soc. Automotive Eng. (SAE) J.,* vol. 1, no. 1, pp. 894-902, 2009.

[19] G., Sulligoi, D. Bosich, G. Giadrossi, L. Zhu, M. Cupelli, et al, "Multiconverter medium voltage DC power systems on ships: constant-power loads instability solution using linearization via state feedback control," *IEEE Trans. Smart Grid*, vol. 5, no. 5, pp. 2543-2552, 2014.

[20] N. Bottrell, M. Prodanovic and T. C. Green, "Dynamic stability of a microgrid with an active load," *IEEE Trans. Power Electron.*, vol. 28, no. 11, pp. 5107-5119, 2013.

[21] A. Emadi, A. Khaligh, C. H. Rivetta and G. A. Williamson, "Constant power loads and negative impedance instability in automotive systems: Definition, modeling, stability, and control of power electronic converters and motor drives," *IEEE Trans. Veh. Technol.*, vol. 55, no. 4, pp. 1112-1125, 2006.

[22] D. Marx, P. Magne, B. Nahid-Mobarakeh, S. Pierfederici and B. Davat, "Large signal stability analysis tools in dc power systems with constant power loads and variable power loads – a review," *IEEE Trans. Power Electron.*, vol. 27, no. 4, pp. 1773-1787, 2012.

[23] J. M. Guerrero, L. García de Vicuña, J. Matas, M. Castilla, et al, "Output impedance design of parallel-connected UPS inverters with wireless load-sharing control," *IEEE Trans. Ind. Electron.*, vol. 52, no. 4, pp. 1126-1135, 2005.

[24] J. He, Y. W. Li and M. S. Munir, "A flexible harmonic control approach through voltage-controlled DG-grid interfacing converters," *IEEE Trans. Ind. Electron.*, vol. 59, no. 1, pp. 444-455, 2012.

[25] A. A. Rockhill, M. Liserre, R. Teodorescu and P. Rodriguez "Grid-filter design for a multimegawatt medium-voltage voltage-source inverter," *IEEE Trans. Ind. Electron.*, vol. 58, no. 4, pp. 1205-1217, 2011.

[26] G. AlLee and W. Tschudi, "Edison Redux: 380 Vdc Brings Reliability and Efficiency to Sustainable Data Centers," *IEEE Power Energy Mag.*, vol. 10, no. 6, pp. 50–59, 2012.

[27] C. M. Wildrick, F. C. Lee, B. H. Cho and B. Choi, "A method of defining the load impedance specification for a stable distributed power system," *IEEE Trans. Power Electron.*, vol. 10, no. 3, pp. 280-285, 1995.

[28] M. Cespedes, L. Xing and J. Sun, "Constant-power load system stabilization by passive damping," *IEEE Trans. Power Electron.*, vol. 26, no. 7, pp. 1832-1836, 2011.

[29] M. Cupelli, L. Zhu and A. Monti, "Why ideal constant power loads are not the worst case condition from a control standpoint," *IEEE Trans. Smart Grid*, to appear.

[30] A. Kwasinski and C. N. Onwuchekwa, "Dynamic behavior and stabilization of dc microgrids with instantaneous constant-power loads," *IEEE Trans. Power Electron.*, vol. 26, no. 3, pp. 822-834, 2011.

[31] W. –J. Lee and S. –Ki Sul, "DC-link voltage stabilization for reduced dc-link capacitor inverter," *in Proc. of IEEE ECCE*, pp.1740-1744, 2009.

[32] P. Magne, B. Nahid-Mobarakeh and S. Pierfederici, "DC-link voltage large signal stabilization and transient control using a virtual capacitor," *in Proc. of IEEE IAS*, pp. 1-8, 2010.

[33] D. Bosich, G. Giadrossi and G. Sulligoi, "Voltage control solutions to face the CPL instability in MVDC shipboard power systems," *in Proc. of AEIT*, pp. 1-6, 2014.

[34] A. –B. Awan, B. Nahid-Mobarakeh, S. Pierfederici and F. Meibody-Tabar, "Nonlinear stabilization of a DC-bus supplying a constant power load," *in Proc. of IEEE IAS*, pp.1-8, 2009.

[35] P. Liutanakul, A. –B. Awan, S. Pierfederici, B. Nahid-Mobarakeh and F. Meibody-Tabar, "Linear stabilization of a DC bus supplying a constant power load: a general design approach," *IEEE Trans. Power Electron.*, vol. 25, no. 2, pp. 475-488, 2010.

[36] V. Arcidiacono, A. Monti and G. Sulligoi, "An innovative generation control system for improving design and stability of shipboard medium-voltage DC integrated power system," *in Proc. of IEEE ESTS*, pp.152-156, 2009.

[37] P. Magne, B. Nahid-Mobarakeh and S. Pierfederici, "A design method for a fault-tolerant multi-agent stabilizing system for dc microgrids with constant power loads," *in Proc. of IEEE ITEC*, pp. 1-6, 2012.

[38] P. Magne, PhD Thesis. [Online] http://docnum.univ-lorraine.fr/public/DDOC_T_2012_0119_MAGNE.pdf.

[39] A. Khaligh, A. Emadi, "Mixed DCM/CCM pulse adjustment with constant power loads," *IEEE Trans. Aerospace and Electronic Systems*, vol. 44, no. 2, pp. 766-782, 2008.

[40] D. W. Hart, *Power Electronics*, New York: McGraw-Hill, 2010.
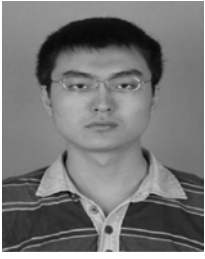
Xiaonan Lu (S'11-M'14) was born in Tianjin, China, 1985. He received the B.E. and Ph.D. degrees in electrical engineering from Tsinghua University, Beijing, China, in 2008 and 2013, respectively. From Sep. 2010 to Aug. 2011, he was a guest Ph.D. student at Department of Energy Technology, Aalborg University, Denmark. From Oct. 2013 to Dec. 2014, he was a postdoc researcher in the Department of Electrical Engineering and Computer Science, University of Tennessee, Knoxville. In Jan. 2015, he joined the Energy Systems Division, Argonne National Laboratory, where he is currently a postdoc appointee.

His research interests are modeling and control of power electronic converters in renewable energy systems and microgrids, hardware-in-the-loop real-time test, multilevel converters, matrix converters, etc. Dr. Lu received the Outstanding Reviewer Award for IEEE Transaction on Power Electronics in 2014.

Dr. Lu is a member of IEEE PELS, IAS and PES Society.

Kai Sun (M'12) was born in Beijing, China, 1977. He received the B.E., M.E., and Ph.D. degrees in electrical engineering all from Tsinghua University, Beijing, China, in 2000, 2002, and 2006, respectively. In 2006, he joined the faculty of Tsinghua University as a Lecturer of Electrical Engineering, where he is currently an Associate Professor. In Sep. 2009-Aug. 2010, Jun.-Jul. 2012 and Jul.-Aug. 2015, he was a Visiting Scholar at Department of Energy Technology, Aalborg University, Denmark.

His main research interests are power converters for renewable generation systems and microgrids. He is the member of the Renewable Energy Systems Technical Committee of the IEEE Industrial Electronics Society and the member of the Sustainable Energy Technical Committee of the IEEE Power Electronics Society. Dr. Sun received the Delta Young Scholar Award in 2013.

Josep M. Guerrero (S'01-M'04-SM'08-F'15) received the B.S. degree in telecommunications engineering, the M.S. degree in electronics engineering, and the Ph.D. degree in power electronics from the Technical University of Catalonia, Barcelona, in 1997, 2000 and 2003, respectively. He was an Associate Professor with the Department of Automatic Control Systems and Computer Engineering, Technical University of Catalonia, teaching courses on digital signal processing, field-programmable gate arrays, microprocessors, and control of renewable energy. In 2004, he was responsible for the Renewable Energy Laboratory, Escola Industrial de Barcelona. Since 2011, he has been a Full Professor with the Department of Energy Technology, Aalborg University, Aalborg East, Denmark, where he is responsible for the microgrid research program. From 2012 he is also a guest professor at the Chinese Academy of Science and the Nanjing University of Aeronautics and Astronautics. From 2013, he is also a guest professor at the Control Science and Engineering College, Shandong University.

His research interests are oriented to different microgrid aspects, including power electronics, distributed energy-storage systems, hierarchical and cooperative control, energy management systems, and optimization of microgrids and islanded minigrids. Prof. Guerrero is an Associate Editor for the IEEE TRANSACTIONS ON POWER ELECTRONICS, the IEEE TRANSACTIONS ON INDUSTRIAL ELECTRONICS, and the IEEE Industrial Electronics Magazine, and an Editor for the IEEE TRANSACTIONS on SMART GRID. He has been Guest Editor of the IEEE TRANSACTIONS ON POWER ELECTRONICS Special Issues: Power Electronics for Wind Energy Conversion and Power Electronics for Microgrids; the IEEE TRANSACTIONS ON INDUSTRIAL ELECTRONICS Special Sections: Uninterruptible Power Supplies systems, Renewable Energy Systems, Distributed Generation and Microgrids, and Industrial Applications and Implementation Issues of the Kalman Filter; and the IEEE TRANSACTIONS on SMART GRID Special Issue on Smart DC Distribution Systems. He was the chair of the Renewable Energy Systems Technical Committee of the IEEE Industrial Electronics Society. In 2014 he was awarded by Thomson Reuters as ISI Highly Cited Researcher.

Juan C. Vasquez (M'12-SM'15) received the B.S. degree in Electronics Engineering from Autonoma University of Manizales, Colombia in 2004 where he has been teaching courses on digital circuits, servo systems and flexible manufacturing systems. In 2009, He received his Ph.D. degree from the Technical University of Catalonia, Barcelona, Spain in 2009 at the Department of Automatic Control Systems and Computer Engineering, from Technical University of Catalonia, Barcelona (Spain), where he worked as Post-doc Assistant and also teaching courses based on renewable energy systems. Currently, he is an Assistant Professor at Aalborg University in Denmark. His research interests include modeling, simulation, networked control systems and optimization for power management systems applied to Distributed Generation in AC/DC Microgrids.

Lipei Huang was born in Jiangsu, China, 1946. He received the B.E. and M.E. degrees in electrical engineering from Tsinghua University, Beijing, China, in 1970 and 1982, respectively, and the Ph.D. degree from Meiji University, Tokyo, Japan, in 1996. In 1970, he joined the Department of Electrical Engineering, Tsinghua University. Since 1994, he has been a Professor in the Department of Electrical Engineering, Tsinghua University. In 1987, he was a Visiting Scholar of Electrical Engineering at the Tokyo Institute of Technology, for three months, and at Meiji University, Kawasaki, Japan, for nine months. He joined the research projects of K. Matsuse Laboratory, Department of Electrical Engineering, Meiji University, Kawasaki, Japan, as a Visiting Professor in 1993.

He has authored more than 100 technical papers and holds 7 patents. His research interests are in power electronics and adjustable-speed drives.

Prof. Huang received the Education Awards from the China Education Commission and Beijing People's Government in 1997. From 2001 to 2003 he was a Delta Scholar.
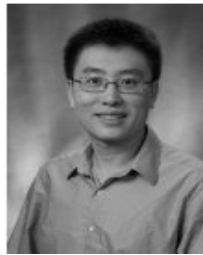
Jianhui Wang (M'07-SM'12) received the Ph.D. degree in electrical engineering from Illinois Institute of Technology, Chicago, IL, USA, in 2007. Presently, he is the Section Lead for Advanced Power Grid Modeling at the Energy Systems Division at Argonne National Laboratory, Argonne, IL, USA.

Dr. Wang is the secretary of the IEEE Power & Energy Society (PES) Power System Operations Committee. He is an associate editor of Journal of Energy Engineering and an editorial board member of Applied Energy. He is also an affiliate professor at Auburn University and an adjunct professor at University of Notre Dame. Dr. Wang is the Editor-in-Chief of the IEEE Transactions on Smart Grid and an IEEE PES Distinguished Lecturer.